Electronic and thermoelectric properties of few-layer transition metal dichalcogenides

Darshana Wickramaratne, Ferdows Zahid, and Roger K. Lake

Citation: The Journal of Chemical Physics **140**, 124710 (2014); doi: 10.1063/1.4869142
View online: http://dx.doi.org/10.1063/1.4869142
View Table of Contents: http://scitation.aip.org/content/aip/journal/jcp/140/12?ver=pdfcov
Published by the AIP Publishing

Electronic and thermoelectric properties of few-layer transition metal dichalcogenides

Darshana Wickramaratne,[1] Ferdows Zahid,[2] and Roger K. Lake[1]
[1]*Department of Electrical Engineering, University of California, Riverside, California 92521-0204, USA*
[2]*Department of Physics and the Center of Theoretical and Computational Physics, The University of Hong Kong, Pokfulam Road, Hong Kong SAR, China*

(Received 2 January 2014; accepted 7 March 2014; published online 31 March 2014)

The electronic and thermoelectric properties of one to four monolayers of MoS_2, $MoSe_2$, WS_2, and WSe_2 are calculated. For few layer thicknesses, the near degeneracies of the conduction band K and Σ valleys and the valence band Γ and K valleys enhance the n-type and p-type thermoelectric performance. The interlayer hybridization and energy level splitting determine how the number of modes within k_BT of a valley minimum changes with layer thickness. In all cases, the maximum ZT coincides with the greatest near-degeneracy within k_BT of the band edge that results in the sharpest turn-on of the density of modes. The thickness at which this maximum occurs is, in general, not a monolayer. The transition from few layers to bulk is discussed. Effective masses, energy gaps, power-factors, and ZT values are tabulated for all materials and layer thicknesses. © *2014 AIP Publishing LLC*. [http://dx.doi.org/10.1063/1.4869142]

I. INTRODUCTION

Semiconducting, transition-metal dichalcogenides (TMDCs) exhibit promising electronic,[1–5] opto-electronic,[6] and spintronic[7] properties. Single monolayers (three atomic layers) can be either exfoliated or grown with chemically stable surfaces. The electronic, optical, and spin properties of monolayers are qualitatively different from those of the bulk. The bandgap changes from indirect to direct, and the valence band edges at the K and K' points become spin polarized.[6,7] These materials are discussed in a number of recent reviews.[8–12]

Experimental studies conducted on a different set of two-dimensional materials, namely, Bi_2Te_3 and Bi_2Se_3, demonstrated an improvement in their thermoelectric performance as their thickness was reduced.[13,14] A large increase in ZT has been theoretically predicted for monolayer Bi_2Te_3 compared to that of the bulk.[15–17] This enhancement in ZT results from the unique, step-function shape of the density of modes at the valence band edge of a single quintuple layer.[16,17] The shape of the density of modes increases the power factor, and the increase in the power factor increases ZT. For Bi_2Te_3, the large enhancement in the power factor and in ZT only occurs for a monolayer. For bilayer and trilayer Bi_2Te_3, the step-like shape of the density of modes disappears, and the calculated values of ZT are either slightly higher[18] or slightly lower[17] than that of the bulk.

Prior experimental and theoretical investigations of the thermoelectric performance of transition metal dichalcogenides have focused on either bulk or monolayer materials.[6,19–24] There has not been a study of the effect of film thickness on the power factor and ZT in the transition metal dichalcogenides. It is not known whether the power factor and ZT are maximum at monolayer thickness or at some other thickness.

This work theoretically investigates the electronic properties and the thermoelectric performance of bulk and one to four monolayers of 4 different TMDC materials: MoS_2, $MoSe_2$, WS_2, and WSe_2. The goal is to understand how their electronic and thermoelectric properties vary with thickness. Similar to monolayer Bi_2Te_3, the increase in ZT for the ultrathin films results from an enhanced degeneracy or near-degeneracy of the band edges. In the TMDCs, at few layer thicknesses, different valleys become nearly degenerate with energy differences of less than k_BT at room temperature. Because of weak interlayer coupling at certain valleys, additional bands from additional layers lie within k_BT of the band edges for few layer thicknesses. The increased degeneracy results in a sharper turn on of the density of modes near the band edges. In all cases, the thickness with the sharpest increase in the density of modes has the largest value for ZT. For the semiconducting TMDCs considered here, that optimum thickness is not, in general, a single monolayer.

II. THEORETICAL METHODS

Ab initio calculations of the bulk and few-layer structures (one to four layers) are carried out using density functional theory (DFT) with a projector augmented wave method[25] and the Perdew-Burke-Ernzerhof (PBE) type generalized gradient approximation[26,27] as implemented in the Vienna *ab initio* simulation package (VASP).[28,29] The vdW interactions in $MoSe_2$ and MoS_2 are accounted for using a semi-empirical correction to the Kohn-Sham energies when optimizing the bulk structures (optimization of WS_2 and WSe_2 structures are done at the PBE level since the semi-empirical parameters for tungsten are currently not described by the dispersion potential).[30] The Monkhorst-Pack scheme is used for the integration of the Brillouin zone with a k-mesh of 12 × 12

$\times$ 6 for the bulk structures and 12 $\times$ 12 $\times$ 1 for the thin films. The energy cutoff of the plane wave basis is 300 eV. All of the electronic band structure calculations include spin-orbit coupling. Calculations are also performed without spin-orbit coupling and the results are compared.

To verify the results of the PBE calculations, the electronic structure of 1L, 2L, 3L, and 4L MoS_2 are calculated using the much more computationally expensive hybrid Heyd-Scuseria-Ernzerhof (HSE) functional.[31] The HSE calculations incorporate 25% short-range Hartree-Fock exchange. The screening parameter μ is set to 0.4 $Å^{-1}$.

The thermoelectric parameters are calculated from a Landauer formalism using the *ab initio* derived density of modes.[16,17,23] In the linear response regime, the electronic conductivity (σ), the electronic thermal conductivity (κ_e), and the Seebeck coefficient (S) are expressed as[32,33]

$$\sigma = (2q^2/h)I_0 \quad (\Omega^{-1}\mathrm{m}^{-1}), \tag{1}$$

$$\kappa_e = \left(2Tk_B^2/h\right)\left(I_2 - I_1^2/I_0\right) \quad (\mathrm{Wm}^{-1}\,\mathrm{K}^{-1}), \tag{2}$$

$$S = -(k_B/q)\frac{I_1}{I_0} \quad (\mathrm{V/K}), \tag{3}$$

with

$$I_j = \frac{1}{L}\int_{-\infty}^{\infty}\left(\frac{E-E_F}{k_BT}\right)^j \bar{T}(E)\left(-\frac{\partial f_0}{\partial E}\right)dE, \tag{4}$$

where L is the device length, q is the magnitude of the electron charge, h is Planck's constant, and k_B is Boltzmann's constant. The transmission function is

$$\bar{T}(E) = T(E)M(E), \tag{5}$$

where M(E) as the density of modes (DOM). In the diffusive limit,

$$T(E) = \lambda(E)/L, \tag{6}$$

and $\lambda(E)$ is the electron mean free path. When phonon scattering is dominant, the mean free path can be written as a constant, $\lambda(E) = \lambda_0$. As discussed in Ref. 34, the transport distribution, $\Xi(E)$, arising from the Boltzmann transport equation is related to the above quantities by $\Xi(E) = \frac{2}{h}T(E)M(E)$.

The density of modes M(E) can be defined as[17,32]

$$M(E) = \left(\frac{L_\perp}{2\pi}\right)^{d-1}\int_{BZ}\sum_{k_\perp}\Theta(E-\epsilon(k_\perp))dk_\perp^{d-1}, \tag{7}$$

where d is the dimensionality of the system, $L_\perp$ are the dimensions of the structure perpendicular to the direction of transport ($L_\perp^2$ = W $\times$ t for d = 3, $L_\perp$ = W for d = 2; W = width of the structure, t = film thickness), Θ is the unit step function, and $k_\perp$ refers to the k states in the first Brillouin zone perpendicular to the transport direction. Using Eq. (7), M(E) of any material in any dimension can be numerically evaluated from a given electronic band structure by counting the bands that cross the energy of interest. The density of modes calculations are performed by integrating over the first Brillouin zone using a converged k point grid (51 $\times$ 51 $\times$ 10 k points for the bulk structures and 51 $\times$ 51 $\times$ 1 for the thin films).

We account for carrier scattering within each structure by fitting our calculated bulk electrical conductivity with bulk experimental data. An electron mean free path of λ_0 = 14 nm gives the best agreement with experimental data on the Seebeck response of bulk MoS_2 as a function of the electrical conductivity.[35,36] The bulk p-type electrical conductivity of MoS_2 at room temperature was reported to be 5.1 Ω^{-1} cm^{-1} with a Seebeck coefficient of ~450 μVK^{-1} at a carrier concentration of 10^{16} cm^{-3}.[36] Using λ_0 = 14 nm we obtain an electrical conductivity of 4.97 Ω^{-1} cm^{-1} with a Seebeck coefficient of ~398 μVK^{-1} at the same carrier concentration. This value of the mean free path is also consistent with a theoretically derived energy independent acoustic phonon-limited mean free path (λ_0 = 14 nm) for electrons in monolayer MoS_2,[37] and was successfully used to simulate and compare to experimental results of the transfer characteristics of single layer MoS_2 field effect transistor.[2] As an initial approximation of carrier scattering we use the same λ_0 value to model the thermoelectric properties of all the TMDC materials investigated in this study.

For the in-plane lattice thermal conductivity, a κ_l value of 19.5 $\mathrm{Wm}^{-1}\,\mathrm{K}^{-1}$ obtained from a molecular dynamics simulation on monolayer MoS_2 is used.[38] Prior experimental[39] and theoretical[23] studies of the lattice thermal conductivity in the TMDC materials have demonstrated that κ_L does not vary significantly for the different TMDC compounds studied here. With the above quantities in hand, the power factor, $S^2\sigma$, and the thermoelectric figure of merit $ZT = S^2\sigma T/(\kappa_l + \kappa_e)$ are determined.

III. RESULTS

All of the thermoelectric parameters are derived from the calculated electronic band structures. Therefore, we begin this section with a discussion of the calculated band structures. The band structure calculations produce considerably more information than is required for calculating the thermoelectric parameters. To preserve that information and contribute towards a database of material parameters, extracted properties such as effective masses and energy gaps at high symmetry points are tabulated.

Figure 1 shows the *ab initio* band structure of one-layer (1L) through four-layer (4L) and bulk WS_2. The large valence band splitting at the K-point and the direct-indirect gap transition as the film thickness increases above 1L are features that occur in the other TMDC materials included as part of this study. The last panel in Fig. 1 illustrates the effect of decreasing layer thickness on the bandgap for all of the materials studied. The optimized lattice parameters of the bulk TMDC compounds are listed in Table I. The results in Table I and Figure 1 are consistent with prior experimental characterization[40–42] and theoretical calculations of the bulk[43,44] and thin film[46,47] crystal structures and electronic band structures. The results of these electronic structure calculations at the high symmetry points are summarized in Tables II and III. Table II gives the relative effective masses, and Table III gives the energy gaps.

A number of prior theoretical studies of the electronic structure of monolayer and few-layer TMDCs did not include

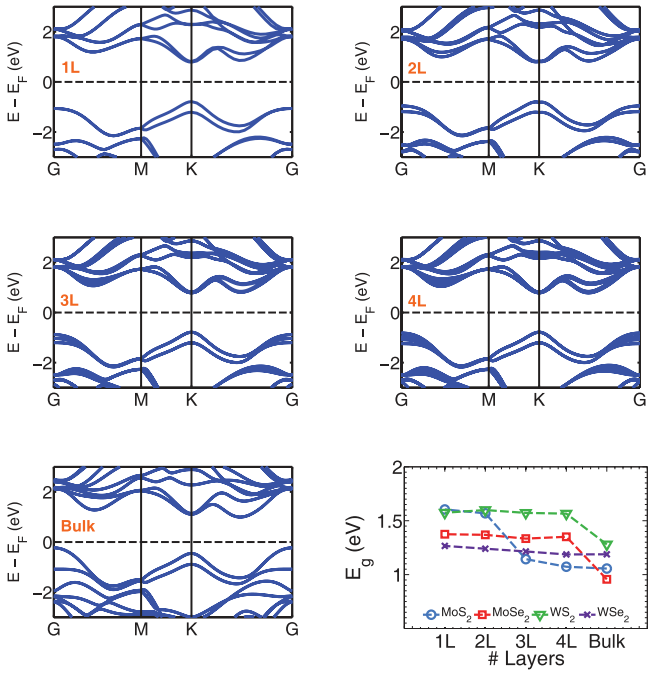

FIG. 1. *Ab initio* calculated band structures of WS_2: 1L, 2L, 3L, 4L, and bulk. The bottom right panel illustrates the variation of the bandgap of the TMDC materials as a function of the number of layers.

spin-orbit interaction.[45–47] As a result, the bandgaps reported in those studies are slightly larger. For example, the bandgaps reported in a prior PBE level calculation[47] are greater by 70 meV, 260 meV, and 284 meV for MoS_2 and $MoSe_2$, WS_2, and WSe_2, respectively, when compared to our calculation results. Without the inclusion of spin-orbit interaction, our values for the bandgap of the monolayer TMDCs are consistent with the bandgaps reported in these studies. Including spin-orbit coupling results in a splitting of the valence bands, Δ_{SO}, at K. The spin orbit interaction shifts up one of the degenerate valence bands, and this reduces the bandgap. The degree of the energy shift ranges from 39.6 meV for MoS_2 to 210.9 meV for WS_2. The second degenerate valence band is shifted down by an energy that is also unique to each TMDC material; this ranges from 110.4 meV for MoS_2 to 316.2 meV for WSe_2. For example, the calculated Δ_{SO} energies of the monolayer TMDCs are 150 meV, 181 meV, 425 meV, and 461 meV for MoS_2, $MoSe_2$, WS_2, and WSe_2, respectively. This is in good agreement with a prior PBE level calculation[48] that accounted for spin-orbit interaction which obtained Δ_{SO} values of 146 meV, 183 meV, 425 meV, and 461 meV for MoS_2, $MoSe_2$, WS_2, and WSe_2, respectively, and a Δ_{SO} energy of 188 meV obtained for monolayer MoS_2 with the use of optical absorption experiments.[49]

More sophisticated many-body *ab initio* calculations which include HSE or GW calculations have been reported in prior studies of the band structure of monolayer[48,50,51,53] and bilayer[51,53] structures of the molybdenum and tungsten dichalcogenides. The values for Δ_{SO} resulting from these theories are only slightly changed from those of the PBE model. The Δ_{SO} values reported for monolayer MoS_2, $MoSe_2$, WS_2, and WSe_2 with a GW (HSE) calculation are 164 (193) meV, 212 (261) meV, 456 (521) meV, and 501 (586) meV.[48] The primary difference between the PBE and the HSE and GW calculations is an increase in the bandgap. However, the PBE bandgap is large enough compared to the temperatures considered that the exact magnitude of the bandgap has no effect on the thermoelectric parameters. An explicit comparison of the electronic structure and the thermoelectric parameters calculated from the PBE and the HSE functionals for 1L - 4L MoS_2 is given below.

Calculation of the thermoelectric parameters requires the density of modes extracted from the electronic band structure using Eq. (7). Figure 2 shows the density of modes versus energy for bulk, 1L, 2L, 3L, and 4L MoS_2, $MoSe_2$, WS_2, and WSe_2. To compare the density of modes of the bulk structure with the thin-film structures, we divide the density of modes of the thin-film structures by their respective thickness, t. As will be shown, for these TMDCs, small variations in the shape of the density of modes near the band edges can enhance the power factor and subsequently ZT. The thermoelectric properties of the bulk and thin-film structures are calculated from Eqs. (1)–(6) using the density of modes shown in Fig. 2.

The Seebeck coefficient, electrical conductivity, power-factor (PF), and the thermoelectric figure-of-merit (ZT) as a function of the reduced Fermi level, η_F are shown in Figures 3–6, respectively. The reduced Fermi-level is $\eta_F = \frac{E_F - E_{C1}}{kT}$ for electrons in the conduction band, and $\eta_F = \frac{E_F - E_{V1}}{kT}$ for holes in the valence band. E_{C1} and E_{V1} are the energies of the conduction and valence band edges, respectively. For each material and each thickness the maximum power factor and ZT occurs for the conduction band states. The peak conduction band and valence band power factor and ZT for each structure and material at 77 K, 150 K, and 300 K are summarized in Tables IV and V, respectively. For all materials, the few layer structures show a large increase in the values of their power factor and ZT compared to those of the bulk.

The peak n-type ZT values (and corresponding layer thicknesses) for MoS_2, $MoSe_2$, WS_2, and WSe_2 are 2.23

TABLE I. Calculated properties of bulk TMDC materials: lattice constant a_0, c-axis lattice constant c_0, z-parameter z, and bandgap E_g(eV). Experimental values[40–42] have been included for comparison.

	a_0(Å)	c_0(Å)	z	a_0^{expt}(Å)	c_0^{expt}(Å)	z^{expt}	E_g(eV)	E_g^{expt}(eV)
MoS_2	3.179	12.729	0.627	3.160	12.290	0.629	1.060	1.29
$MoSe_2$	3.309	13.323	0.624	3.289	12.927	0.621	0.959	1.09
WS_2	3.183	13.131	0.630	3.150	12.320	0.622	1.283	1.35
WSe_2	3.319	13.729	0.627	3.282	12.960	0.621	1.188	1.20

TABLE II. *Ab initio* calculations of the hole and electron effective masses at the valence band maxima and conduction band minima, respectively, for each structure in units of the free electron mass (m_0). The subscripts l and t refer to the masses calculated at the symmetry point along the longitudinal and the transverse directions.

Structure	Point	MoS_2	$MoSe_2$	WS_2	WSe_2	MoS_2	$MoSe_2$	WS_2	WSe_2
		Hole effective mass (m_0)				**Electron effective mass (m_0)**			
1L	K_l	0.543	0.578	0.339	0.341	0.506	0.502	0.349	0.345
	K_t	0.546	0.588	0.339	0.348	0.504	0.503	0.347	0.345
2L	Γ	1.039	1.430	1.239	1.322	…	…	…	…
	K_l	0.548	0.595	0.345	0.349	0.521	0.539	0.359	0.411
	K_t	0.546	0.596	0.346	0.348	0.510	0.539	0.359	0.412
3L	Γ	1.239	1.432	1.246	1.382	…	…	…	…
	K_t	0.549	0.602	0.366	0.368	0.559	0.544	0.376	0.434
	K_t	0.548	0.604	0.366	0.368	0.559	0.544	0.377	0.434
4L	Γ	1.239	1.433	1.351	1.432	…	…	…	…
	K_l	0.548	0.604	0.366	0.367	0.554	0.542	0.376	0.435
	K_t	0.546	0.604	0.366	0.368	0.559	0.549	0.377	0.434
Bulk	Γ	0.838	0.973	0.832	0.997	…	…	…	…
	Σ_l	…	…	…	…	0.590	0.521	0.569	0.489
	Σ_t	…	…	…	…	0.845	0.776	0.665	0.643

(t = 3L), 2.39 (t = 2L), 2.03 (t = 3L), and 1.91 (t = 2L) which is an improvement by a factor of 6.4, 8.2, 7.2, and 7.5 over the respective bulk values. These peak ZT values occur when the Fermi level is moved by 1.39 kT, 1.55 kT, 1.08 kT, and 1.39 kT, respectively, below the conduction band at T = 300 K. This corresponds to electron carrier densities of 6.26×10^{19} cm^{-3}, 5.74×10^{19} cm^{-3}, 5.34×10^{19} cm^{-3}, and 4.72×10^{19} cm^{-3} for MoS_2, $MoSe_2$, WS_2, and WSe_2, respectively. The peak p-type ZT values (and corresponding layer thicknesses) for MoS_2, $MoSe_2$, WS_2, and WSe_2 are 1.15 (t = 2L), 0.81 (t = 2L-4L), 0.76 (t = 2L-3L), and 0.62 (t = 1L-4L) which is an improvement by a factor of 14.4, 10.1, 9.5, and 5.2 over the respective bulk values. These peak ZT values occur when the Fermi level is moved by 1.16 kT, 1.01 kT, 0.93 kT, and 0.85 kT, respectively, above the valence band at T = 300 K. This corresponds to hole carrier densities

TABLE III. *Ab initio* calculations of the bandgap energies and energy transitions between the valence (v) and conduction (c) band valleys for each structure and material. The splitting of the valence band at the K-point due to spin-orbit coupling and the inter-layer interactions are denoted as K_{v1} and K_{v2}. Σ is the mid-point between Γ and K. The bandgap at each dimension is highlighted in bold text. Experimental values when available[40–42,59] have been included for comparison. (Note: The bandgap of 2L, 3L, and 4L WSe_2 occurs between the K_{v1} and Σ_C. The 2L, 3L, and 4L bandgaps of WSe_2 are 1.216 eV, 1.1594 eV, and 1.1345 eV, respectively.)

Structure	Transition	MoS_2	$MoSe_2$	WS_2	WSe_2	MoS_2	$MoSe_2$	WS_2	WSe_2
		Calculated (eV)				**Expt. (eV)**			
1L	Γ_v to K_c	1.705	1.768	1.849	1.776	…	…	…	…
	Γ_v to Σ_c	1.922	1.862	1.929	1.806	…	…	…	…
	K_{v1} to K_c	**1.600**	**1.375**	**1.573**	**1.254**	1.900	1.660	1.950	1.640
	K_{v2} to K_c	1.750	1.556	1.973	1.715	2.050	1.850	2.360	2.040
2L	Γ_v to K_c	**1.564**	**1.368**	**1.507**	1.586	1.600	…	1.730	…
	Γ_v to Σ_c	1.775	1.373	1.542	1.562	…	…	…	…
	K_{v1} to K_c	1.600	1.373	1.549	1.269	1.880	…	1.910	1.590
	K_{v2} to K_c	1.760	1.556	1.977	1.788	2.050	…	2.340	2.000
3L	Γ_v to K_c	**1.150**	**1.334**	**1.458**	1.586	…	…	…	…
	Γ_v to Σ_c	1.171	1.372	1.482	1.508	…	…	…	…
	K_{v1} to K_c	1.620	1.376	1.485	1.265	…	…	…	…
	K_{v2} to K_c	1.780	1.564	1.873	1.783	…	…	…	…
4L	Γ_v to K_c	**1.120**	**1.351**	**1.438**	1.546	…	…	…	…
	Γ_v to Σ_c	1.139	1.374	1.439	1.434	…	…	…	…
	K_{v1} to K_c	1.630	1.356	1.459	1.259	…	…	…	…
	K_{v2} to K_c	1.780	1.574	1.877	1.753	…	…	…	…
Bulk	Γ_v to Σ_c	**1.060**	**0.959**	**1.283**	**1.188**	1.290	1.090	1.350	1.200
	K_{v1} to K_c	1.590	1.349	1.453	1.258	1.880	1.350	1.880	1.580
	K_{v2} to K_c	1.780	1.588	1.889	1.737	2.060	1.380	2.320	1.950

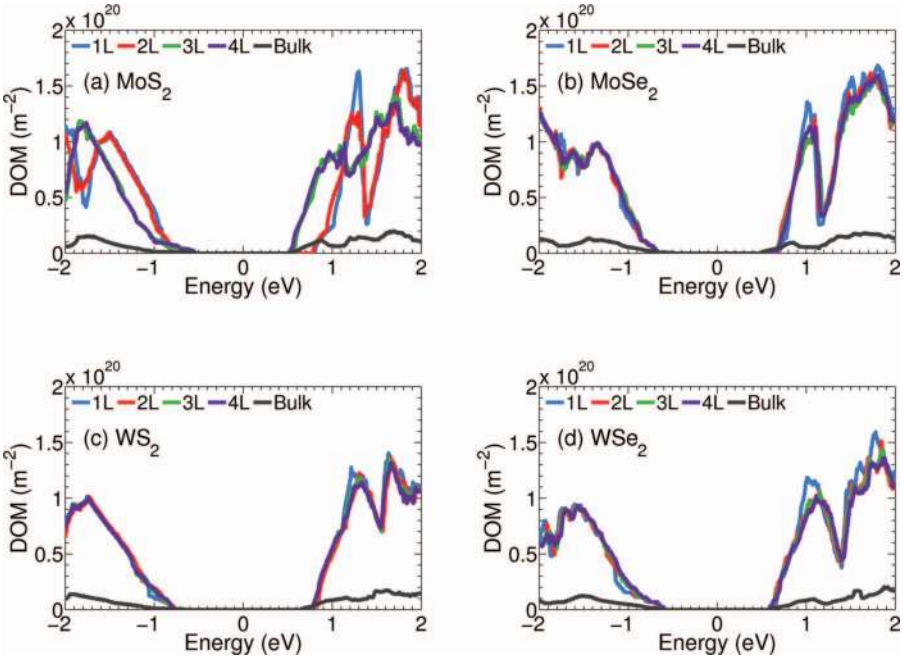

FIG. 2. Distribution of modes per unit area versus energy for (a) MoS_2, (b) $MoSe_2$, (c) WS_2, and (d) WSe_2 for bulk (black), 1L (blue), 2L (red), 3L (green), and 4L (purple) structures. The midgap energy is set to E = 0.

of 7.12×10^{19} cm^{-3}, 5.84×10^{19} cm^{-3}, 4.02×10^{19} cm^{-3}, and 3.91×10^{19} cm^{-3} for MoS_2, $MoSe_2$, WS_2, and WSe_2, respectively. Of the four TMDC materials studied, MoS_2 is the only material to exhibit a p-type and n-type ZT > 1. In contrast to Bi_2Te_3, the peak value of ZT does not occur in any of the materials at a monolayer thickness.

The Seebeck coefficients at the maximum n-type (p-type) ZT for each material are 275 (245.6) μVK^{-1}, 287 (230.7) μVK^{-1}, 279 (230.1) μVK^{-1}, and 276 (216.7) μVK^{-1} for MoS_2, $MoSe_2$, WS_2, and WSe_2, respectively. However, the Seebeck coefficients at the maximum n-type (p-type) power factor for each material are 167 (90.4) μVK^{-1}, 100 (185.8) μVK^{-1}, 165 (177.1) μVK^{-1}, and 171 (172.1) μVK^{-1} for MoS_2, $MoSe_2$, WS_2, and WSe_2, respectively. This is generally consistent with the conclusion of a report on engineering the Seebeck coefficient to obtain the maximum thermoelectric power factor.[52]

Without the inclusion of spin-orbit interaction our values of the ballistic ZT for the monolayer TMDC materials are consistent with a prior report on the monolayer thermoelectric properties of these TMDC materials.[23] Our calculations show that without the inclusion of spin-orbit interaction the peak n-type ZT values for all materials continue to occur at thicknesses above a single monolayer. The peak

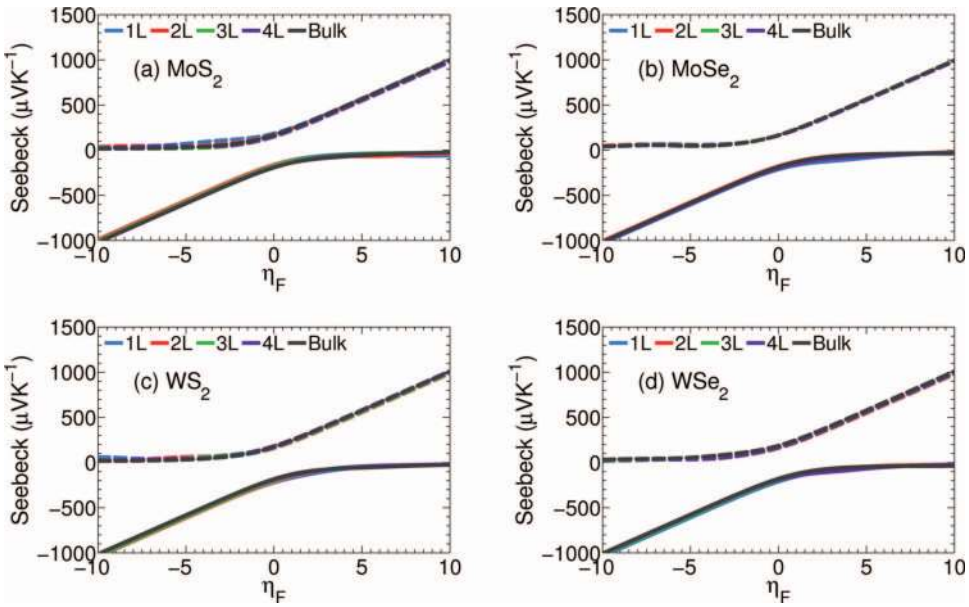

FIG. 3. Seebeck coefficient at 300 K for (a) MoS_2, (b) $MoSe_2$, (c) WS_2, and (d) WSe_2 for bulk (black), 1L (blue), 2L (red), 3L (green), and 4L (purple) structures. The n-type Seebeck coefficients are plotted with a solid line and p-type coefficients with a broken line as a function of the reduced Fermi energy, η_F.

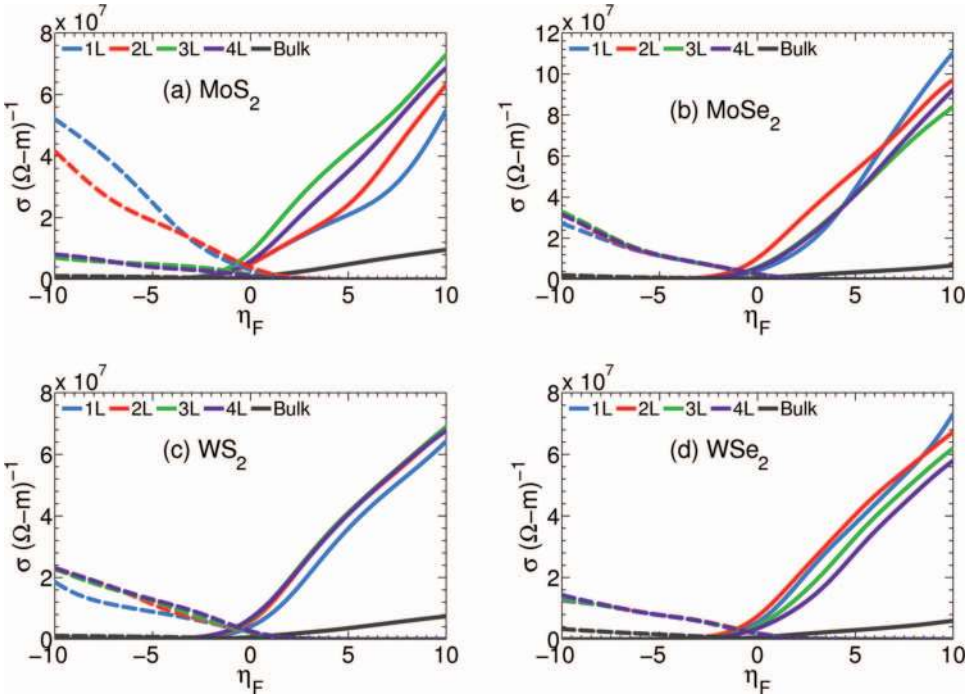

FIG. 4. Electrical conductivity, σ, at 300 K for (a) MoS_2, (b) $MoSe_2$, (c) WS_2, and (d) WSe_2 for 1L (blue), 2L (red), 3L (green), and 4L (purple) and bulk (black) structures. The n-type electrical conductivity is plotted with a solid line and p-type conductivity with a broken line as a function of the reduced Fermi energy, η_F.

n-type ZT values (and corresponding layer thicknesses) without spin-orbit interaction for MoS_2, $MoSe_2$, WS_2, and WSe_2 are 1.38 (t = 3L), 1.52 (t = 2L), 1.13 (t = 4L), and 1.28 (t = 2L). However, the peak p-type ZT values without spin-orbit interaction occurs for a single monolayer for each TMDC material. The p-type ZT values without spin-orbit interaction for MoS_2, $MoSe_2$, WS_2, and WSe_2 are 1.42, 0.84, 0.90, and 0.69.

Recent electronic structure calculations using the Heyd-Scuseria-Ernzerhof (HSE) hybrid functional[53] give a bandgap that more accurately matches known experimental values.[53] To assess whether the trends in the thermoelectric parameters predicted with the PBE functional are the same as those resulting from the HSE functional, we calculate the electronic band structure of 1L, 2L, 3L, and 4L MoS_2 with both the PBE and the HSE functional and plot the results in Fig. 7. Near the

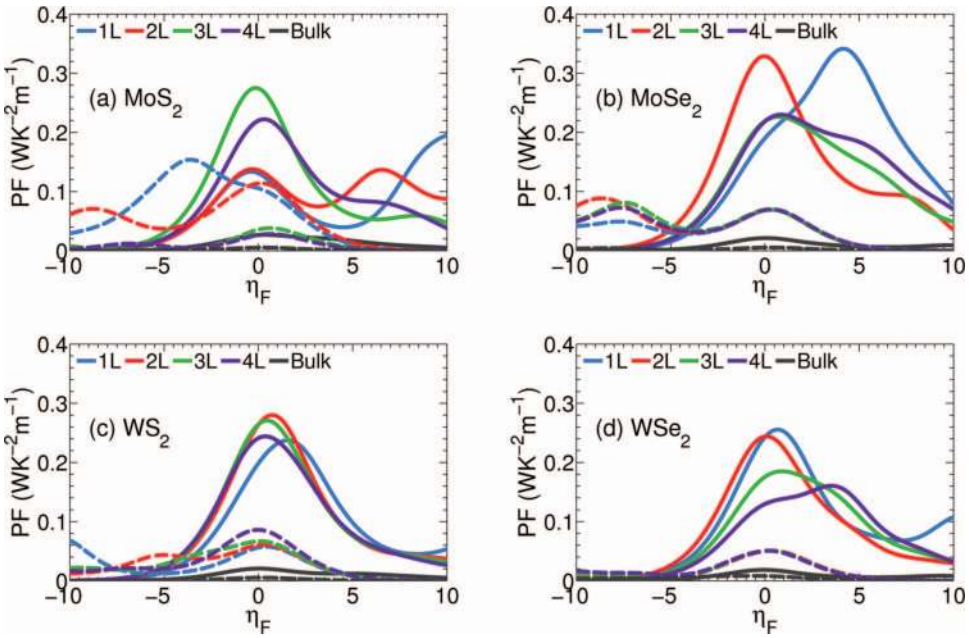

FIG. 5. Power factor (PF) at 300 K for (a) MoS_2, (b) $MoSe_2$, (c) WS_2, and (d) WSe_2 for bulk (black), 1L (blue), 2L (red), 3L (green), and 4L (purple) structures. The n-type power factors are plotted with a solid line and p-type PFs with a broken line as a function of the reduced Fermi energy, η_F.

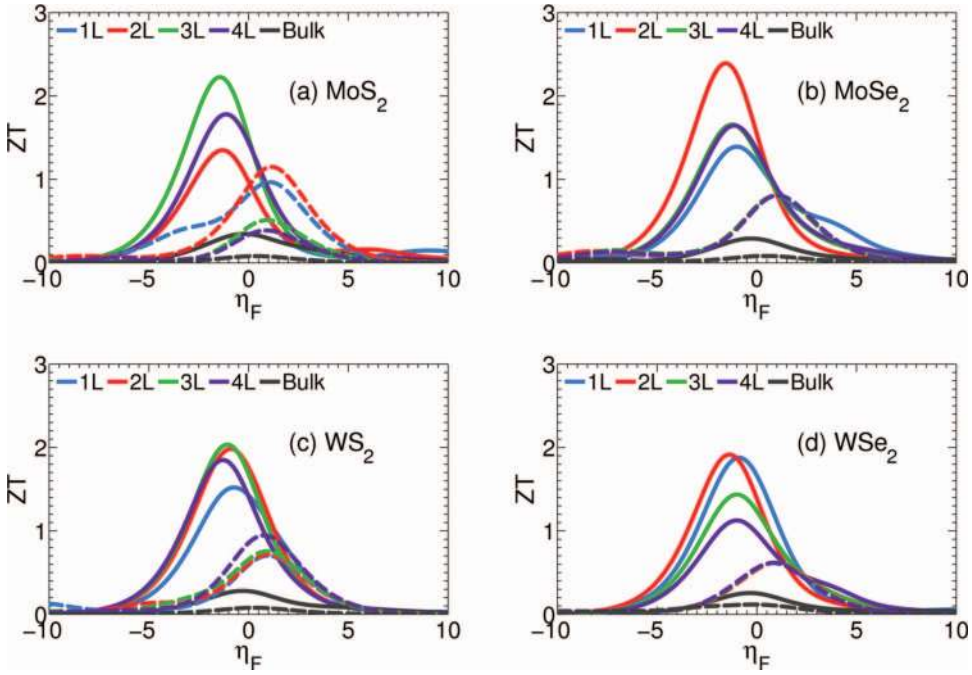

FIG. 6. ZT at 300 K for (a) MoS_2, (b) $MoSe_2$, (c) WS_2, and (d) WSe_2 for bulk (black), 1L (blue), 2L (red), 3L (green), and 4L (purple) structures. The n-type ZT is plotted with a solid line and p-type ZT with a broken line as a function of the reduced Fermi energy, η_F.

TABLE IV. Peak n-type (p-type) power factor of 1L, 2L, 3L, 4L and bulk MoS_2, $MoSe_2$, WS_2, and WSe_2 at 300 K, 150 K, and 77 K. The maximum power factor for each material at a given temperature is in bold.

	Temperature	1L	2L	3L	4L	Bulk
		Maximum n-type (p-type) power factor ($WK^{-2}\,m^{-2}$)				
MoS_2	300 K	0.130 (0.150)	0.140 (0.110)	**0.280** (0.041)	0.220 (0.031)	0.0320 (0.010)
	150 K	0.093 (0.072)	0.093 (0.071)	**0.190** (0.032)	0.120 (0.024)	0.012 (0.0042)
	77 K	0.072 (0.043)	0.072 (0.053)	**0.13** (0.021)	0.063 (0.022)	0.012 (0.0031)
$MoSe_2$	300 K	**0.340** (0.071)	0.330 (0.094)	0.230 (0.082)	0.230 (0.071)	0.022 (0.0061)
	150 K	**0.151** (0.050)	0.200 (0.051)	0.100 (0.051)	0.100 (0.052)	0.013 (0.004)
	77 K	**0.062** (0.031)	0.120 (0.032)	0.062 (0.031)	0.052 (0.032)	0.013 (0.0032)
WS_2	300 K	0.240 (0.062)	**0.280** (0.061)	0.270 (0.071)	0.240 (0.092)	0.022 (0.0052)
	150 K	0.110 (0.042)	**0.160** (0.042)	0.150 (0.041)	0.130 (0.051)	0.010 (0.0043)
	77 K	0.051 (0.031)	**0.081** (0.032)	0.070 (0.032)	0.081 (0.031)	0.010 (0.0022)
WSe_2	300 K	**0.260** (0.054)	0.240 (0.052)	0.190 (0.053)	0.160 (0.053)	0.022 (0.014)
	150 K	**0.141** (0.030)	0.140 (0.031)	0.081 (0.031)	0.070 (0.031)	0.010 (0.004)
	77 K	0.071 (0.031)	**0.082** (0.031)	0.050 (0.031)	0.043 (0.022)	0.011 (0.0021)

TABLE V. Peak n-type (p-type) thermoelectric figure of merit, ZT, of 1L, 2L, 3L, 4L and bulk MoS_2, $MoSe_2$, WS_2, and WSe_2 at 300 K, 150 K, and 77 K. The maximum ZT for each material at a given temperature is in bold.

	Temperature	1L	2L	3L	4L	Bulk
		Maximum n-type (p-type) ZT				
MoS_2	300 K	1.35 (0.970)	1.35 (1.15)	**2.23** (0.510)	1.78 (0.390)	0.350 (0.081)
	150 K	0.590 (0.350)	0.590 (0.450)	**1.03** (0.220)	0.660 (0.160)	0.110 (0.034)
	77 K	0.240 (0.140)	0.240 (0.190)	**0.420** (0.093)	0.210 (0.062)	0.031 (0.012)
$MoSe_2$	300 K	1.39 (0.800)	**2.39** (0.810)	1.66 (0.810)	1.65 (0.810)	0.290 (0.081)
	150 K	0.450 (0.310)	**1.06** (0.320)	0.610 (0.320)	0.570 (0.320)	0.100 (0.033)
	77 K	0.130 (0.120)	**0.410** (0.120)	0.220 (0.120)	0.170 (0.120)	0.030 (0.014)
WS_2	300 K	1.52 (0.70)	1.98 (0.720)	**2.03** (0.760)	1.85 (0.760)	0.280 (0.082)
	150 K	0.411 (0.280)	0.613 (0.280)	**0.770** (.280)	0.721 (0.350)	0.104 (0.030)
	77 K	0.120 (0.110)	0.181 (0.113)	0.211 (0.113)	**0.271** (0.113)	0.034 (0.012)
WSe_2	300 K	1.88 (0.620)	**1.92** (0.620)	1.44 (0.620)	1.13 (0.620)	0.260 (0.120)
	150 K	0.590 (0.220)	**0.750** (0.220)	0.490 (0.220)	0.380 (0.220)	0.091 (0.032)
	77 K	0.180 (0.100)	**0.270** (0.100)	0.170 (0.100)	0.130 (0.100)	0.031 (0.014)

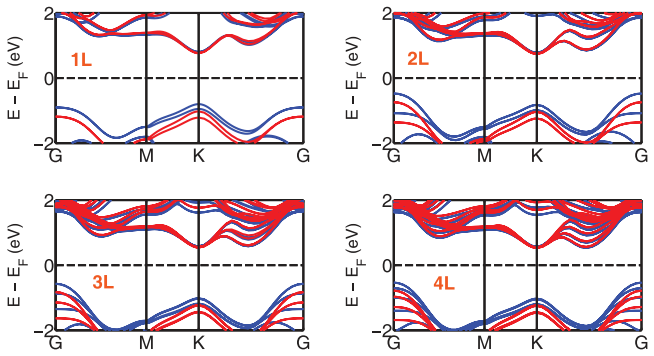

FIG. 7. *Ab initio* calculated electronic structure of MoS_2: 1L, 2L, 3L, and 4L structures using a PBE (blue) and hybrid HSE (red) functional. The HSE functional provides a correction to the underestimated PBE bandgap while the salient features of the electronic structure that would affect the density-of-modes calculation remain the same.

band edges, the HSE energies appear to be shifted with respect to the PBE energies. The effective masses for the HSE band structures are lower by up to 17% for the conduction band valleys at K and Σ and are lower by up to 11% for the valence band valleys at K and Γ.

To verify that the HSE functional leaves the thermoelectric trends predicted from the PBE functional unchanged, we compute the density-of-modes and thermoelectric performance of 1L, 2L, and 3L MoS_2 using the HSE functional with the inclusion of spin orbit coupling. Figure 8 illustrates the DOM, Seebeck coefficient, power factor, and ZT for the 1L, 2L, and 3L structures of MoS_2 computed with the HSE functional. The quantitative values do differ. For the MoS_2 trilayer structure, the HSE (PBE) functionals give a peak n-type power factor of 0.41 (0.28) $WK^{-2}m^{-2}$ and a peak n-type ZT of 2.4 (2.2). However, the HSE results for few-layer MoS_2 structures demonstrate the same trends in the shape of the density of modes and the same trends in the values for the power factors and ZT. Both the HSE and PBE calculations show that the turn-on of the density of modes is sharpest for the tri-layer structure resulting in maximum values for the power factor and ZT. Since the primary effect on the low energy states of the exact exchange in the HSE functional is to shift the band edges with respect to those of a PBE calculation, the trends resulting from the shape of the density of modes should be preserved.

Figure 9 summarizes the values from the PBE calculations for the peak n-type and p-type ZT and power factors for each TMDC material and layer thickness. In the n-type $MoSe_2$, WS_2, and WSe_2 structures, the peak power-factor, and the peak ZT do not occur at the same film thickness. For example, in $MoSe_2$, a single monolayer has the highest power factor, and a bilayer has the highest ZT. This can be explained by the increase in the electronic thermal conductivity, κ_e as the Fermi level is moved into the conduction band.

Figure 10 shows the ratio of the total thermal conductivity, κ_{tot}, with respect to the lattice thermal conductivity, κ_l, for each TMDC material. The two guide lines on each figure illustrate the reduced Fermi level position at which the maximum n-type power factor and ZT occurs. The ratio $\kappa_{tot}/\kappa_l = 1 + \kappa_e/\kappa_l$ is higher at the Fermi level position where the maximum power factor occurs. This increase in κ_e explains why the peak power factor and ZT occur at different Fermi energies and film thicknesses.

A number of recent studies report on the theoretical[54,55] and experimental values[56,57] of the lattice thermal conductivity on monolayer and few-layer TMDC materials with values of κ_l ranging from 19 $Wm^{-1}K^{-1}$ to 83 $Wm^{-1}K^{-1}$. Experimental measurements of the in-plane κ_l in suspended samples of MoS_2[57] find a value of 34.5 $Wm^{-1}K^{-1}$ for 1L MoS_2 and 52 $Wm^{-1}K^{-1}$ for few-layer MoS_2. To assess whether the inequivalent κ_l values for the monolayer and few-layer TMDC

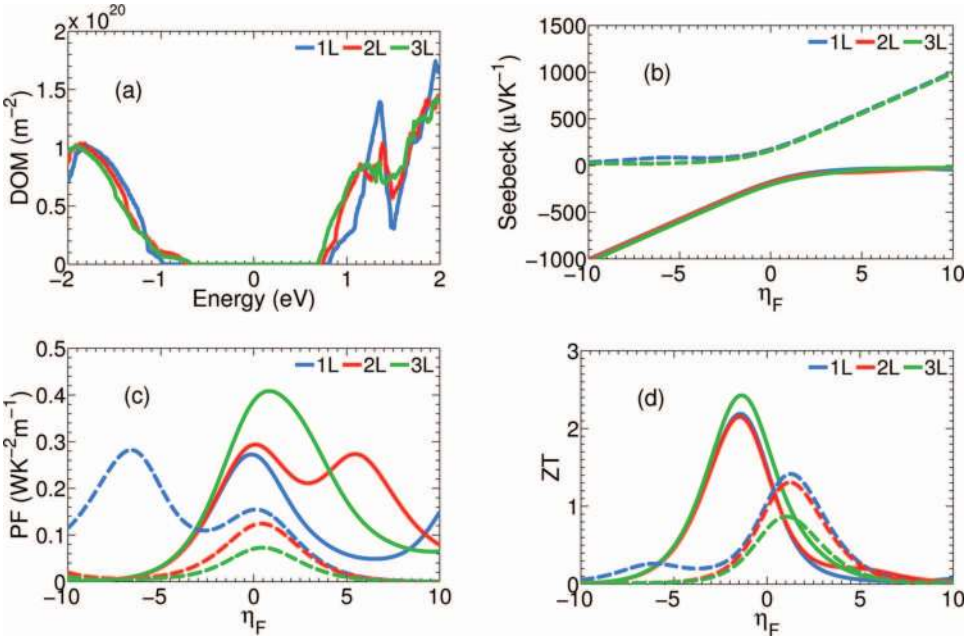

FIG. 8. HSE calculation of the (a) density-of-modes, (b) Seebeck coefficient, (c) Power factor, and (d) ZT 1L (blue), 2L (red), 3L (green) MoS_2. The n-type thermoelectric parameters are plotted with a solid line and the p-type parameters are plotted with a broken line as a function of the reduced Fermi energy, η_F.

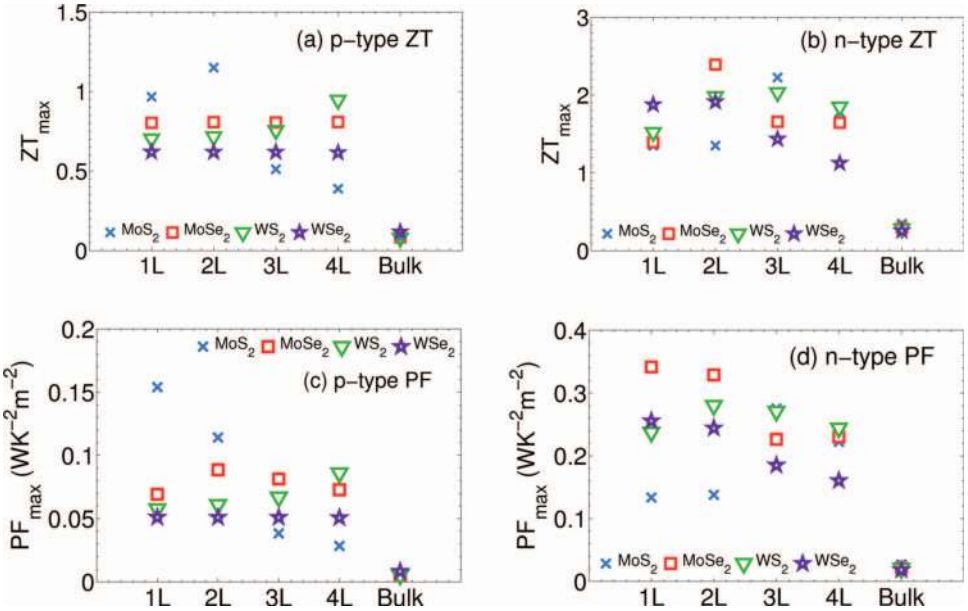

FIG. 9. Maximum thermoelectric performance for 1L (blue), 2L (red), 3L (green), 4L (purple), and bulk (black) MoS_2, $MoSe_2$, WS_2, WSe_2 at 300 K: (a) maximum p-type ZT, (b) maximum n-type ZT, (c) maximum p-type power factor, (d) maximum n-type power factor.

films leave the predicted thermoelectric trends unchanged, we computed the thermoelectric parameters using $\kappa_l = 34.5$ $Wm^{-1}K^{-1}$ for the monolayer and $\kappa_l = 52$ $Wm^{-1}K^{-1}$ for the few-layer TMDC films of each material. The values of ZT differ compared to using $\kappa_l = 19$ $Wm^{-1}K^{-1}$ for each film thickness. For MoS_2, the room temperature n-type ZT values using the thickness dependent (constant) κ_l for the 1L, 2L, 3L, and 4L structures are 0.87 (1.35), 0.63 (1.15), 1.11 (2.23), 0.89 (1.78). The maximum n-type ZT still occurs for the 3L structure and the minimum n-type ZT still occurs for the 1L structure. The trends for all of the n-type materials are preserved when a thickness dependent thermal conductivity is used. All of the values are shown in Fig. 11(b). For the n-type materials, changes in the density of modes are the dominant factor determining the trends. For p-type $MoSe_2$, WS_2, WSe_2, ZT varies little for different layer thicknesses when using a constant κ_l as shown in Fig. 9(a). For p-type MoS_2, the difference between the maximum ZT of a bilayer and the second

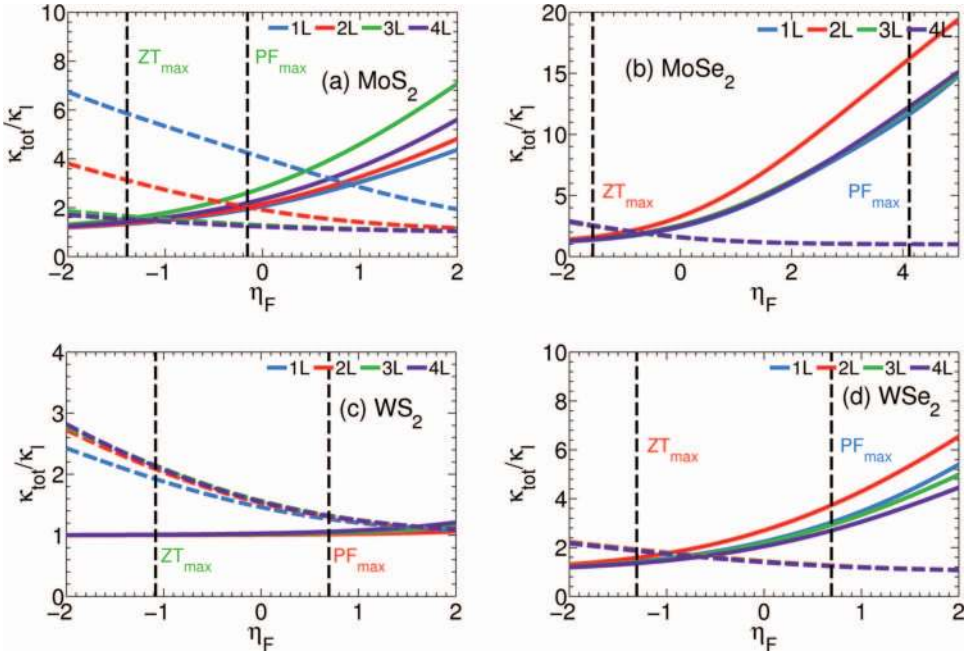

FIG. 10. Ratio of total thermal conductivity (κ_l+κ_e) over the lattice thermal conductivity (κ_l) at 300 K for (a) MoS_2, (b) $MoSe_2$, (c) WS_2, (d) WSe_2 for 1L (blue), 2L (red), 3L (green), and 4L (purple) structures. The n-type ratio is plotted with a solid line and p-type ratio with a broken line as a function of the reduced Fermi energy, η_F. The two vertical dashed lines show the reduced Fermi level position at which the maximum n-type power factor and ZT occur.

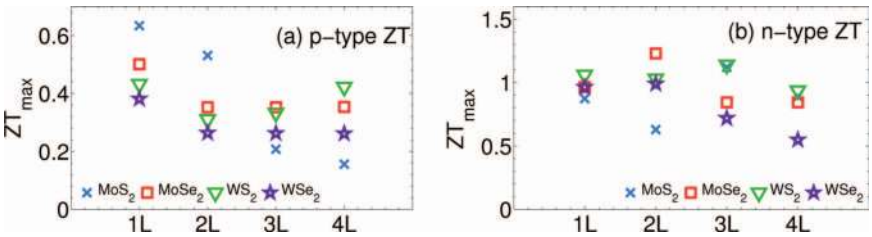

FIG. 11. Maximum ZT for (a) p-type and (b) n-type of MoS_2, $MoSe_2$, WS_2, WSe_2 at 300 K for 1L (blue), 2L (red), 3L (green), 4L (purple) structures accounting for thickness-dependent lattice thermal conductivity. $\kappa_l = 34.5\ \mathrm{Wm^{-1}\,K^{-1}}$ used for the 1L structures and $\kappa_l = 52\ \mathrm{Wm^{-1}\,K^{-1}}$ used for the few-layer structures.

highest value of a monolayer is small. Therefore, reducing the value of κ_l for a monolayer from 52 to 35.4 $\mathrm{WM^{-1}\,K^{-1}}$ is sufficient to cause the peak value of ZT to occur at monolayer thickness for all 4 p-type materials as shown in Fig. 11(a).

In an attempt to study the transition of the thermoelectric performance from few-layer films to bulk like performance, we calculate the thermoelectric parameters for an 8L film of WS_2. Figure 12 illustrates the density of modes and the ZT for bulk, 3L and 8L WS_2. The n-type 0.974 ZT value of the 8L film is a factor of 1.9 smaller than that of the 4L film, but it is still a factor of 3.5 larger than that of the bulk. The p-type 0.163 ZT value of the 8L film is a factor of 4.7 smaller than that of the 4L film, and it is a factor of 2.0 larger that that of the bulk. Even at 8 monolayers, there is still an enhancement of the ZT value compared to that of the bulk, and the enhancement is larger in the n-type material.

The thermoelectric performance in the low dimensional structures is enhanced by the more abrupt step-like shape of the density of modes distribution.[34] It is clear from Eq. (4), that with $E_F \leq 0$, a step-function density of modes removes all negative contributions to the integrand of I_1 giving a maximum value for I_1. The conduction band DOM distribution for the maximum and minimum ZT structures for each material are plotted in Figure 13. In all cases, the DOM with the sharper turn-on at the band edge gives rise the maximum value for ZT.

IV. DISCUSSION

The enhancement in the thermoelectric performance of *few* monolayer TMDC materials is in contrast to the enhanced thermoelectric performance observed for only a single quintuple (QL) layer of p-type Bi_2Te_3. Above 1 QL of Bi_2Te_3, the thermoelectric figure of merit approaches the bulk ZT.[16,17] The enhancement of ZT in n-type monolayer Bi_2Te_3 is minimal. This difference in the effect of layer thickness on ZT in the two different classes of materials can be explained by differences in the effect of thickness on the band-edge degeneracy and the density of modes. The valence band of monolayer Bi_2Te_3 is a ring in k-space that covers much of the Brillouin zone as shown in Fig. 4(d) of Ref. 17. Thus, the integration over $k_\perp$ in Eq. (7) jumps from zero in the bandgap to a finite number at the band edge resulting in a step-function turn-on of the valence band density of modes as seen in Fig. 3 of Ref. 16 and Fig. 2 of Ref. 17. The size of the ring in k-space quickly collapses for thicknesses above a monolayer, and the large enhancement in ZT dissappears. In a parabolic band, the band edge is a point in k-space, and, in two-dimensions, the density of modes turns on smoothly as $\sqrt{E}$.[34] The band edge of n-type monolayer Bi_2Te_3 remains parabolic resulting in a smooth turn-on of the density-of-modes and no significant enhancement of ZT.

The bands of the TMDC materials also remain parabolic at the band edges, however the conduction bands at the K_c and the Σ_c valleys become nearly degenerate for few monolayer thicknesses as shown in Fig. 1. Since the Σ_c valley is 6-fold degenerate, and the K_c valley is 2-fold degenerate, this results in a near 8-fold degeneracy of the conduction band edge. This increases the density of modes in the conduction band by a factor of 8 from that of a single valley. Furthermore, with increasing film thickness from 1L to 4L, the splitting of the Σ_c bands resulting from interlayer coupling is on the order of k_BT. In MoS_2, the splitting at Σ_C is 0.4 meV for the 2L and 40 meV for the 4L structure. The other materials show similar magnitudes of the energy splitting as a function of thickness. Therefore, the near-degeneracy of the bands at Σ_c increases linearly with the film thickness, so that the number of modes

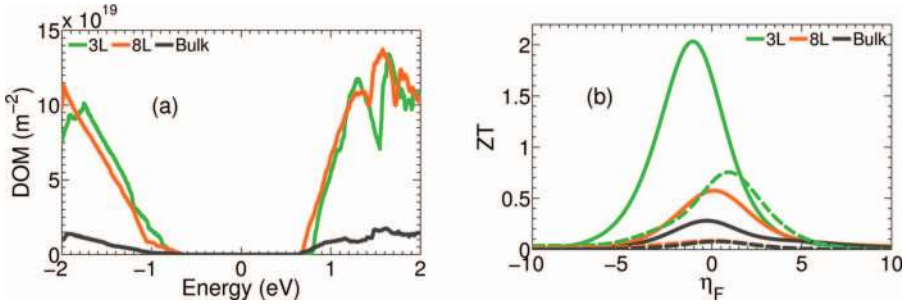

FIG. 12. (a) Density of modes and (b) ZT as a function of the reduced Fermi level for 3L (green), 8L (orange), and bulk (bulk) WS_2.

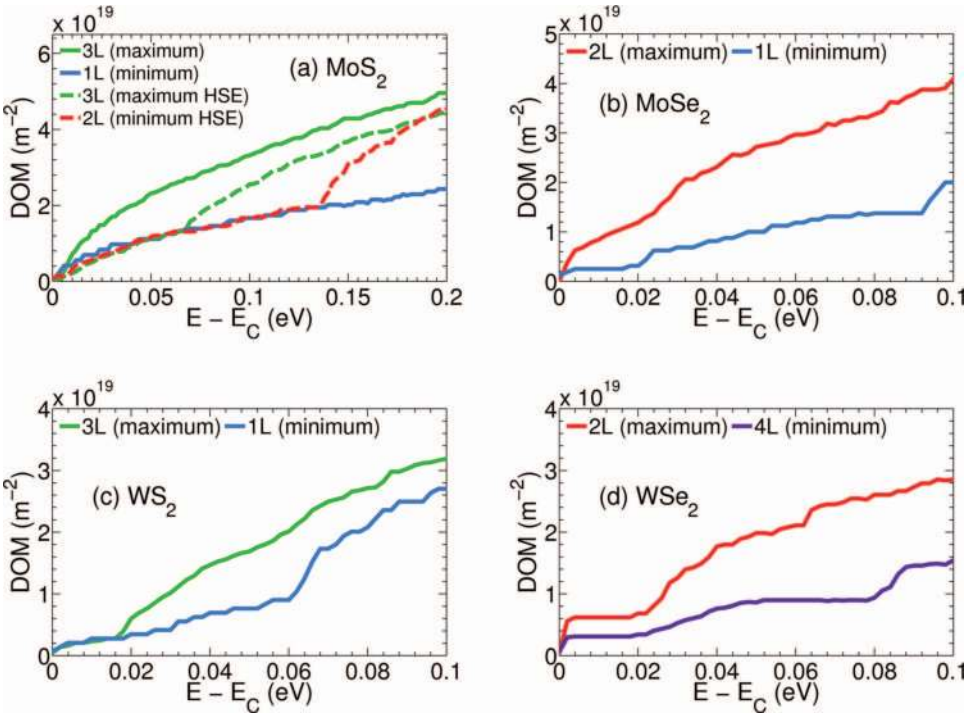

FIG. 13. Conduction band density of modes (DOM) for (a) MoS_2, (b) $MoSe_2$, (c) WS_2, and (d) WSe_2 at film thicknesses where the maximum and the minimum ZT occurs with respect to the energy away from the conduction band edge, E_C.

per layer becomes relatively insensitive to the layer thickness for few monolayer thicknesses.

The interlayer coupling of the out-of-plane d_{z^2} and p_z orbitals result in the strongest interlayer hybridization and energy level splitting.[58] In MoS_2 the orbital composition of the conduction band Σ_c valley is 36% d_{z^2}, 22% d_{xy}, 23% $d_{x^2-y^2}$, 6% p_z, and 5% p_x and p_y. The d-orbital composition of the K_c valley is 67% d_{z^2}. With increasing layer number, the K_c valley splitting is larger than k_BT so that the number of modes contributed by the K_c valleys remains 3 independent of layer number. Thus, when the Σ_c valley falls within k_BT of the K_c valley, its contribution to the density of modes dominates for few-layer thicknesses. Beyond 4 layers, the total splitting becomes larger than 2 k_BT, and the number of accessible modes at Σ_c no longer increases linearly with thickness.

Beyond a monolayer, the valence band shifts to Γ_v for MoS_2, $MoSe_2$, and WS_2. The energy difference between Γ_v and K_v varies as a function of the film thickness and material. For MoS_2 the energy difference between Γ_v and K_v increases from 35 meV for the bilayer to 470 meV and 510 meV for the 3L and 4L structures, respectively. The near degeneracy of the Γ_v and K_v valleys leads to the largest p-type density of modes for 2L MoS_2. For $MoSe_2$, the Γ_v and K_v valleys are nearly degenerate above a single monolayer. In WS_2, the energy difference of the Γ_v and K_v valleys decreases from 42 meV to 21 meV as the film thickness is increased from a bilayer to four layers. For WSe_2, the valence band maxima continues to reside at K_v beyond a monolayer. Once the valence band K_v valleys begin to contribute in $MoSe_2$, WS_2, and WSe_2, the density of modes per layer becomes relatively independent of layer thickness, since there is little splitting of the K_v valleys due to the interlayer coupling.[58] The K_v valley orbital composition contains no d_{z^2} or p_z components. In MoS_2, the splitting varies from 0.2 meV for the 2L structure to 7.6 meV for the 4L structure. The other materials show similar magnitudes of the energy splitting as a function of thickness. Thus, at room temperature, the number of contributed modes per layer within k_BT of the K_v valley minimum remains constant for thicknesses in the range of one to four monolayers.

For the 8 layer WS_2 structure, the conduction band K_c and Σ_c valleys are still nearly degenerate. The K_c valley lies 21 meV above the Σ_c valley. However, at both valleys, the total splitting of the 8 bands contributed from the 8 layers is much greater than k_BT at room temperature. At Σ_c, only two of the 8 bands are within 26 meV of the valley minimum. The overall energy splitting of the 8 bands at Σ_c is 193 meV. In the valence band, the K_v valley is 22 meV below the Γ_v valley. However, the 8 bands from the 8 monolayers are split over a total range of 180 meV, and the second band is 40 meV below the K_v valley maximum. Thus, as the number of layers increase, the total energy splitting of the bands contributed from each layer increases, and the number of modes per layer within k_BT of the valley minimums decreases.

As the number of layers becomes macroscopic such that the crystal is periodic in all three dimensions, the total splitting of the bands evolves into the width of the dispersive band along k_z for the bulk crystal. For bulk WS_2, the width of the band along the vertial k_z direction from Σ_c to R at the top of the Brillouin zone is 208 meV which is 15 meV larger than the total splitting of the 8 layer stack. Furthermore, in the bulk, the K_c valley is 126 meV above the Σ_c minimum, so the K_c contributes no modes to the density of modes near the conduction band edge. In the valence band, the K_v valley maximum is 225 meV below the Γ_v maximum, so that the density of

modes near the valence band edge, is entirely from the Γ_v valley. The lack of valley near-degeneracy and the width of the bulk dispersive bands along k_z, result in a minimum density of modes per layer near the band edges compared to those of few layer structures. The reduced number of modes per layer within k_BT of the band edges results in reduced per-layer values of the thermoelectric figure of merit.

For both material systems Bi_2Te_3 and the semiconducting TMDCs, the enhancement of ZT results from the increased degeneracy or near-degeneracy of the band edges. The origin and nature of the degeneracy is different. In the Bi_2Te_3, the valence band edge becomes inverted into a ring as a result of the coupling of the topological surface states. In the TMDCs at few-layer thicknesses, different valleys become nearly degenerate. In the conduction band, the Σ_c valleys become nearly degenerate with the K_c valleys, and they contribute 6 more modes to the 2 modes from the K_c valleys. In the valence band, the K_v valleys become nearly degenerate with the Γ_v, and they contribute 2 more modes. Furthermore, because of the weak interlayer coupling at K_v and Σ_c, the additional bands from additional layers lie within k_BT of the band edges for few layers. The increased band-edge degeneracy results in a sharper turn-on of the density of modes and an increased value of ZT.

V. SUMMARY

The electronic structure of one to four monolayers of the semiconducting transition metal dichalcogenides MoS_2, $MoSe_2$, WS_2, WSe_2 are calculated using DFT with spin-orbit coupling and the PBE functional. Comparisons are made to results in the absence of spin-orbit coupling, and the PBE results are compared to HSE calculations for MoS_2. The peak n-type value of ZT increases by a factor of 6–8 over the bulk value for all materials. Among the 4 materials and 4 thicknesses, bilayer $MoSe_2$ gives the maximum n-type ZT value of 2.4. The peak p-type value of ZT increases by a factor of 5–14 over the bulk value for all materials. The maximum p-type ZT value of 1.2 occurs for bilayer MoS_2. The maximum power factor generally occurs for a different layer thickness and at a more degenerate Fermi level than the maximum value of ZT. This difference can be explained by the increased electrical thermal conductivity at the Fermi level corresponding to the maximum power factor. For all materials, the maximum value of ZT coincides with the sharpest turn-on of the density of modes distribution at the band edge. The sharper turn-on is driven by the near valley degeneracy of the conduction band K_c and Σ_c valleys and the valence band Γ_v and K_v valleys. For few layer structures, the degeneracy is enhanced by the weak interlayer coupling at the Σ_c and K_v valleys.

ACKNOWLEDGMENTS

This work is supported in part by the National Science Foundation (NSF) Grant Nos. 1124733 and 1128304 and the Semiconductor Research Corporation (SRC) Nanoelectronic Research Initiative as a part of the Nanoelectronics for 2020 and Beyond (NEB-2020) program, FAME, one of six centers of STARnet, a Semiconductor Research Corporation program sponsored by MARCO and DARPA, and the University Grant Council (Contract No. AoE/P-04/08) of the Government of HKSA (F.Z.). This work used the Extreme Science and Engineering Discovery Environment (XSEDE), which is supported by NSF, Grant No. OCI-1053575.

[1] B. Radisavljevic, A. Radenovic, J. Brivio, V. Giacometti, and A. Kis, Nat. Nanotechnol. **6**, 147 (2011).
[2] Y. Yoon, K. Ganapathi, and S. Salahuddin, Nano Lett. **11**, 3768 (2011).
[3] H. Fang, S. Chuang, T. C. Chang, K. Takei, T. Takahashi, and A. Javey, Nano Lett. **12**, 3788 (2012).
[4] K. Alam and R. K. Lake, IEEE Trans. Electron Devices **59**, 3250 (2012).
[5] A. N. Han Liu and P. Ye, ACS Nano **6**, 8563 (2012).
[6] T. Li and G. Galli, J. Chem. Phys. C **111**, 16192 (2007).
[7] D. Xiao, G.-B. Liu, W. Feng, X. Xu, and W. Yao, Phys. Rev. Lett. **108**, 196802 (2012).
[8] K. S. Novoselov and A. H. C. Neto, Physica Scr. **2012**, 014006.
[9] Q. H. Wang, K. Kalantar-Zadeh, A. Kis, J. N. Coleman, and M. S. Strano, Nat. Nanotech. **7**, 699 (2012).
[10] A. Geim and I. Grigorieva, Nature **499**, 419 (2013).
[11] M. Xu, T. Liang, M. Shi, and H. Chen, Chem. Rev. **113**, 3766 (2013).
[12] S. Z. Butler, S. M. Hollen, L. Cao, Y. Cui, J. A. Gupta, H. R. Gutirrez, T. F. Heinz, S. S. Hong, J. Huang, A. F. Ismach, *et al.*, ACS Nano **7**, 2898 (2013).
[13] Y. Sun, H. Cheng, S. Gao, Q. Liu, Z. Sun, C. Xiao, C. Wu, S. Wei, and Y. Xie, J. Am. Chem. Soc. **134**, 20294 (2012).
[14] V. Goyal, D. Teweldebrhan, and A. A. Balandin, Appl. Phys. Lett. **97**, 133117 (2010).
[15] P. Ghaemi, R. S. K. Mong, and J. E. Moore, Phys. Rev. Lett. **105**, 166603 (2010).
[16] F. Zahid and R. Lake, Appl. Phys. Lett. **97**, 212102 (2010).
[17] J. Maassen and M. Lundstrom, Appl. Phys. Lett. **102**, 093103 (2013).
[18] F. Zahid and R. K. Lake, personal communication (2011).
[19] A. Amara, Y. Frongillo, M. J. Aubin, S. Jandl, J. M. Lopez-Castillo, and J. P. Jay-Gerin, Phys. Rev. B **36**, 6415 (1987).
[20] H. Imai, Y. Shimakawa, and Y. Kubo, Phys. Rev. B **64**, 241104(R) (2001).
[21] H. Guo, T. Yang, P. Tao, Y. Wang, and Z. Zhang, J. Appl. Phys. **113**, 013709 (2013).
[22] M. Buscema, M. Barkelid, V. Zwiller, H. S. J. van der Zant, G. A. Steele, and A. Castellanos-Gomez, Nano Lett. **13**, 358–363 (2013).
[23] W. Huang, H. Da, and G. Liang, J. Appl. Phys. **113**, 104304 (2013).
[24] C. Lee, J. Hong, M.-H. Whangbo, and J. H. Shim, Chem. Mater. **25**, 3745 (2013).
[25] P. E. Blöchl, Phys. Rev. B **50**, 17953 (1994).
[26] J. P. Perdew, K. Burke, and M. Ernzerhof, Phys. Rev. Lett. **77**, 3865 (1996).
[27] M. Ernzerhof and G. E. Scuseria, J. Chem. Phys. **110**, 5029 (1999).
[28] G. Kresse and J. Hafner, Phys. Rev. B **48**, 13115 (1993).
[29] G. Kresse and J. Furthmuller, Comput. Mater. Sci. **6**, 15 (1996).
[30] S. Grimme, J. Comput. Chem. **27**, 1787 (2006).
[31] J. Heyd, G. E. Scuseria, and M. Ernzerhof, J. Chem. Phys. **118**, 8207 (2003).
[32] C. Jeong, R. Kim, M. Luisier, S. Datta, and M. Lundstrom, J. Appl. Phys. **107**, 023707 (2010).
[33] A. Paul, S. Salamat, C. Jeong, G. Klimeck, and M. Lundstrom, J. Comput. Electron. **11**, 56 (2012).
[34] R. Kim, S. Datta, and M. S. Lundstrom, J. Appl. Phys. **105**, 034506 (2009).
[35] R. Mansfield and S. A. Salam, Proc. Phys. Soc., London, Sect. B **66**, 377 (1953).
[36] S. Thakurta and A. Dutta, J. Phys. Chem. Solids **44**, 407 (1983).
[37] K. Kaasbjerg, K. S. Thygesen, and K. W. Jacobsen, Phys. Rev. B **85**, 115317 (2012).
[38] V. Varshney, S. S. Patnaik, C. Muratore, A. K. Roy, A. A. Voevodin, and B. L. Farmer, Comput. Mater. Sci. **48**, 101 (2010).
[39] C. Chiritescu, D. G. Cahill, N. Nguyen, D. Johnson, A. Bodapati, P. Keblinski, and P. Zschack, Science **315**, 351 (2007).
[40] K. Bronsema, J. De Boer, and F. Jellinek, Z. Anorg. Allg. Chem. **540**, 15 (1986).
[41] W. Schutte, J. D. Boer, and F. Jellinek, J. Solid State Chem. **70**, 207 (1987).
[42] K. K. Kam and B. A. Parkinson, J. Phys. Chem. **86**, 463 (1982).
[43] H. Jiang, J. Phys. Chem. C **116**, 7664 (2012).
[44] R. Coehoorn, C. Haas, J. Dijkstra, C. J. F. Flipse, R. A. de Groot, and A. Wold, Phys. Rev. B **35**, 6195 (1987).

[45]L. Liu, S. Bala Kumar, Y. Ouyang, and J. Guo, IEEE Trans. Electron Devices **58**, 3042 (2011).
[46]A. Kuc, N. Zibouche, and T. Heine, Phys. Rev. B **83**, 245213 (2011).
[47]Y. Ding, Y. Wang, J. Ni, L. Shi, S. Shi, and W. Tang, Phys. B **406**, 2254 (2011).
[48]A. Ramasubramaniam, Phys. Rev. B **86**, 115409 (2012).
[49]K. F. Mak, C. Lee, J. Hone, J. Shan, and T. F. Heinz, Phys. Rev. Lett. **105**, 136805 (2010).
[50]T. Cheiwchanchamnangij and W. R. Lambrecht, Phys. Rev. B **85**, 205302 (2012).
[51]H. Shi, H. Pan, Y.-W. Zhang, and B. I. Yakobson, Phys. Rev. B **87**, 155304 (2013).
[52]P. Pichanusakorn and P. R. Bandaru, Appl. Phys. Lett. **94**, 223108 (2009).
[53]F. Zahid, L. Liu, Y. Zhu, J. Wang, and H. Guo, AIP Adv. **3**, 052111 (2013).
[54]W. Li, J. Carrete, and N. Mingo, Appl. Phys. Lett. **103**, 253103 (2013).
[55]Y. Cai, J. Lan, G. Zhang, and Y.-W. Zhang, Phys. Rev. B **89**, 035438 (2014).
[56]C. Muratore, V. Varshney, J. J. Gengler, J. J. Hu, J. E. Bultman, T. M. Smith, P. J. Shamberger, B. Qiu, X. Ruan, A. K. Roy, *et al.*, Appl. Phys. Lett. **102**, 081604 (2013).
[57]R. Yan, J. R. Simpson, S. Bertolazzi, J. Brivio, M. Watson, X. Wu, A. Kis, T. Luo, A. R. Hight Walker, and H. G. Xing, ACS Nano **8**, 986 (2014).
[58]H.-P. Komsa and A. V. Krasheninnikov, Phys. Rev. B **88**, 085318 (2013).
[59]H. Zeng, G.-B. Liu, J. Dai, Y. Yan, B. Zhu, R. He, L. Xu, S. Xu, X. Chen, and X. Cui, Nat. Sci. Rep. **3**, 1608 (2013).